Progress In Electromagnetics Research B, Vol. 112, 121–133, 2025 PIER B

(Received 11 January 2025, Accepted 24 February 2025, Scheduled 5 July 2025)

A Four-Element Conformal MIMO Antenna with Time-Domain Analysis for UWB Applications

Sandeep Kiran Vattiprolu* and Pullagura Rajesh Kumar

Department of ECE, AU College of Engineering (A), Andhra University, Visakhapatnam, Andhra Pradesh, India

ABSTRACT: This paper presents the design of a four-element conformal Multi-Input Multi-Output (MIMO) antenna system for Ultra-Wideband (UWB) applications. It is implemented on a flexible RT Duroid 5880 substrate with a relative permittivity of 2.2, a loss tangent of 0.0009, and a thickness of 0.25 mm. It employs a stepped microstrip line-fed guitar-shaped antenna as a single antenna element. The single antenna element is then arranged orthogonally around the four edges of a $63 \times 63\,\mathrm{mm}^2$ substrate to create a 4-element MIMO system. The four antennas, designated as Ant-1 to Ant-4, have their ground planes connected through L-shaped stubs. The prototypes of single antenna element and 4-element MIMO are built to compare the simulation and measurement findings. The single antenna element is tested under flat, X-bend, and Y-bend cases. It achieves -10 dB impedance bandwidth from 3.14 GHz to over 10.6 GHz, a maximum group delay deviation of 2 ns, and a system fidelity factor greater than 80% in all cases. The 4-element MIMO system was also tested in flat and conformal configurations. It covers a minimum -10 dB impedance bandwidth from 3.5 to 10.8 GHz and exhibits mutual coupling below -18 dB. Its equivalent circuit model is also realized. Its diversity analysis shows an envelope correlation coefficient (ECC) below 0.01, diversity gain (DG) near 10 dB, channel capacity loss (CCL) under 0.4 bits/s/Hz, total active reflection coefficient (TARC) below -10 dB, and mean effective gain (MEG) between -3 dB and -12 dB across the operating band.

1. INTRODUCTION

In 2002, the Federal Communications Commission (FCC) allocated unlicensed frequency spectrum from 3.1 GHz to 10.6 GHz for ultra-wideband (UWB) systems. UWB technology offers high data transmission, low power consumption, low emission power levels, and resistance to multipath fading. This makes it ideal for indoor communication, radar, microwave imaging, remote sensing, and body area networks [1, 2]. A wide variety of antenna designs for UWB systems, built on rigid and flexible substrates, has been reported in the literature [3–5]. UWB antennas built on flexible substrates offer light weight and adaptability to curved surfaces, making them the ideal choice for UWB portable systems [6]. UWB systems are classified into impulse radio UWB (IR-UWB) and multi-band orthogonal frequency division multiplexing (MB-OFDM). IR-UWB, known for simplicity, low cost, and energy efficiency, is ideal for indoor wireless communication. To ensure signal fidelity, such systems rely on time-domain analysis with metrics like S_{12}, group delay, pulse width stretch ratio, and system fidelity factor [7–9]. UWB signals are more prone to fading in multipath environments due to the stringent transmission power limit, which degrades overall system performance [10]. MIMO technology in UWB systems exploits multipath propagation to enhance reliability, data throughput, signal-to-noise ratio, interference immunity, and spectrum efficiency, without needing extra power or bandwidth [11]. UWB-MIMO antennas are available in various configurations, such as 2-element [12, 13], 4-element [20–30], 6-element [14], 8-element [15], and 12-element [16] designs. The choice of a particular MIMO configuration depends on factors such as channel conditions, available spectrum, and the desired performance. A 2-element MIMO system is simple, cost-effective, and power-efficient but offers limited throughput and diversity, making it suitable for low-demand scenarios. Higher-order MIMO systems (e.g., 6×6, 8×8) provide high throughput and beamforming but require rich scattering, high power, complex hardware, and high costs. In comparison, 4-element MIMO balances performance, power, cost, and complexity, making it practical for most real-world applications with moderate demands.

Mutual coupling in MIMO systems significantly impacts diversity performance. Studies [17, 18] propose mitigation strategies such as optimized antenna placement, orientation, defective ground structures, parasitic elements, stubs, slots, slits, strips, electromagnetic bandgap structures, neutralization lines, and metamaterials.

Various 4-element UWB-MIMO antennas printed on rigid and flexible substrate materials, featuring both unified and non-unified ground planes, have been reported [4, 20–30]. A shared ground offers a unified reference point for all antennas, enabling accurate signal interpretation. In contrast, separate ground planes can lead to voltage mismatches, instability, and errors. For these reasons, MIMO antennas with a shared ground are preferred for practical systems [19]. UWB-MIMO antenna systems featuring four elements have been extensively studied on both rigid and flexible substrate materials. Designs implemented on rigid substrates have been explored with configurations both without a shared ground [20] and with a common

---

* Corresponding author: Sandeep Kiran Vattiprolu (sandeep.vattiprolu@gmail.com).

doi:10.2528/PIERB25011103

Published by THE ELECTROMAGNETIC ACADEMY

ground plane [21, 22]. Similarly, four-element UWB-MIMO antennas fabricated on flexible substrates have been examined in configurations without a common ground [23, 24] and with a shared ground plane [25–30]. Among them, [20] and [28–30] incorporate time-domain analysis, utilizing metrics such as S_{12} and group delay to assess performance. In this work, a four-element conformal MIMO antenna system is designed and implemented on flexible Rogers RT Duroid 5880. Its time domain, frequency domain, and diversity performance are analyzed under both flat and conformal configurations.

2. SINGLE ELEMENT UWB ANTENNA DESIGN

Figure 1 depicts the geometry of the proposed UWB monopole antenna, which features a guitar-shaped radiator on the top layer of the substrate and a bevel-shaped defected ground structure on the bottom layer. The antenna is excited using a stepped microstrip transmission line with two segments.

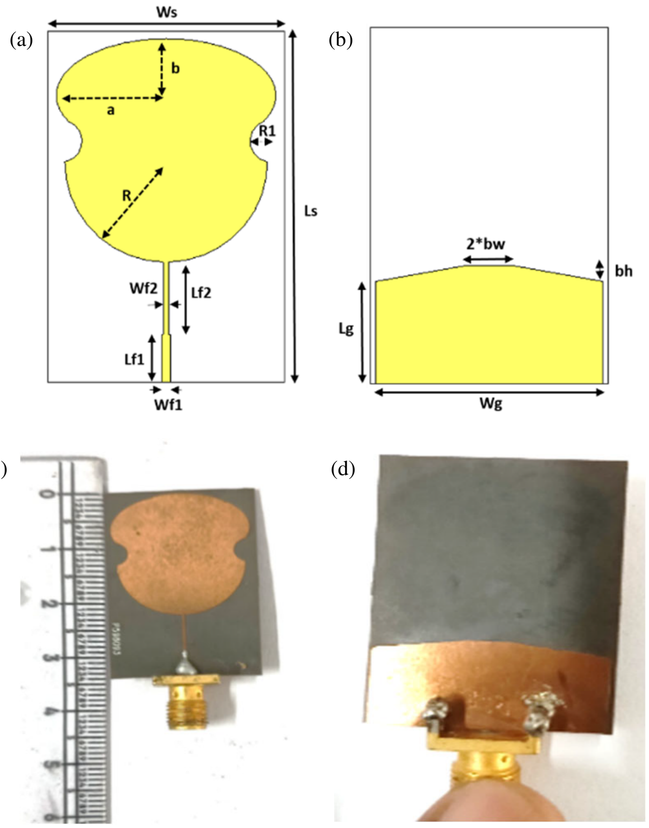

FIGURE 1. Proposed conformal UWB antenna. (a) Simulated model top view, (b) simulated model bottom view, (c) prototype top view, and (d) prototype bottom view.

The first segment is 0.8 mm wide and 4.5 mm long, with an impedance of 50 Ω. The second segment is 0.5 mm wide and 6.8 mm long, with an impedance of 64 Ω. The overall dimensions are $22 \times 33 \times 0.25\,\text{mm}^3$. The single patch and four element MIMO configuration optimized dimensions are listed in Table 1.

The step-by-step evolution of the discussed single antenna element and its reflection coefficient responses are illustrated in Figure 2. The process begins with a simple circular monopole antenna featuring a full ground plane. In the second step, the full ground plane is modified into a partial ground plane to achieve the desired impedance bandwidth. In the third step, a stepped microstrip transmission line is introduced to make the reflection coefficient response shift well below the -10 dB reference line. Next, bevel-shaped cuts are introduced in the partial ground plane to enhance the impedance bandwidth further. In the fifth step, an elliptical structure is added to the upper part of the circular radiator, which moves the lower edge frequency closer to 3.1 GHz. Finally, open circular slots are incorporated on both the right and left sides of the configuration to cover the entire UWB spectrum.

The proposed antenna's lower edge frequency is calculated using (1), as derived in [31].

$$f_L = \frac{7.2}{(L + r)}\,\text{GHz} \tag{1}$$

where L is the height of the radiator which is 2.1 cm, and r is evaluated by equating the total area of the radiator with that of cylindrical wire of height L and radius r. The total area of the radiator is evaluated as below

The area of the circle is given as $A_C = \pi R^2$
The area of the ellipse is given as $A_e = \pi ab$
Where $R = 9.4\,\text{mm}$, $a = 10.2\,\text{mm}$, and $b = 5.35\,\text{mm}$

By using the Monte Carlo method estimated overlapped area between the ellipse and circle is calculated as $A_O = 105.59\,\text{mm}^2$. The circle-shaped slots removed area is $7.5\,\text{mm}^2$.

So, the total area is $A_T = A_C + A_e - A_O - A_S = 277.29 + 171.49 - 105.59 - 7.5 = 335.69\,\text{mm}^2$.

Equating the area of cylindrical wire to that of the radiator $2 \cdot \pi \cdot r \cdot L = 335.69\,\text{mm}^2$, we get r as 2.54 mm.

After substituting the L and r values in Eq. (1), we obtained the lower edge frequency of 3.06 GHz. The measured lower edge frequency is 3.01 GHz. So the percentage of error between the measured and theoretical ones is 1.6%, which is within the error tolerance given in the paper [32].

A parametric study was conducted to understand the effect of geometrical parameter values on the reflection coefficient. During this, one parameter was varied while keeping the others constant. For simplicity, this paper focuses on examining the effects of parameters bh, L_{f1}, L_g, and W_{f2}. In Figure 3(a), variations in bh from its optimal value of 1.5 mm affect the impedance bandwidth, particularly around 5 GHz and 8 GHz, shift resonance frequencies, and alter the resonance depth. Figure 3(b) shows that variations in L_{f1} influence the impedance bandwidth near 5 GHz and 9 GHz, shift the resonance frequencies, and modify the depth of the resonance. In Figure 3(c), adjustments to L_g change the upper cutoff frequency, causing shifts in both the resonance frequency and its depth. Finally, Figure 3(d) demonstrates that changes in W_{f2} affect the antenna's impedance bandwidth and resonance frequencies severely. The proposed antenna's performance is evaluated in the time and frequency domains under three cases: flat, bent along the X-axis on a 10 mm radius cylindrical foam (X-bend), and bent along the Y-axis on a 30 mm radius cylindrical

TABLE 1. Optimized parameters of the MIMO antenna.

	UWB					**UWB-MIMO**		
Parameter	L_s	L_{f1}	L_{f2}	L_g	bh	L	W	d
Values (mm)	33	4.5	6.8	9.5	1.5	63	63	10.25
Parameter	W_s	W_{f1}	W_{f2}	W_g	bw	Sw	Sl	St
Values (mm)	22	15	2.8	21	2	7.6	15.6	0.3
Parameter	R_1	R	a	b		W_1	L_1	t
Values (mm)	2	9.4	10.2	5.35		10	10	2

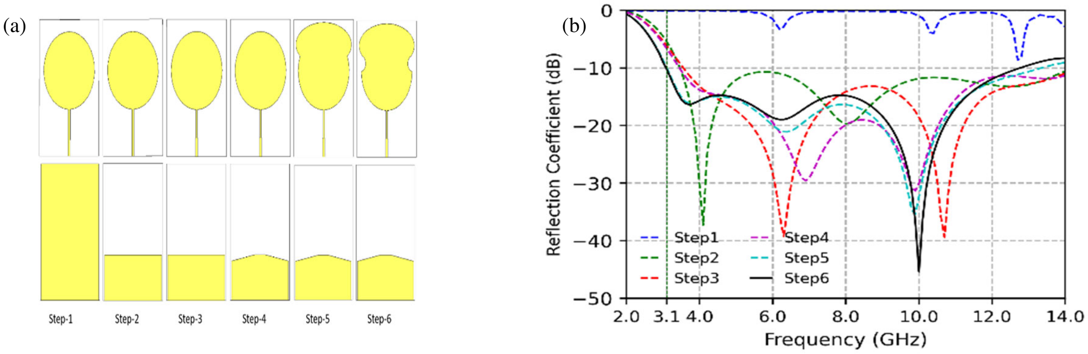

FIGURE 2. (a) Conformal UWB antenna evolution stages and (b) reflection coefficient responses at each evolution step.

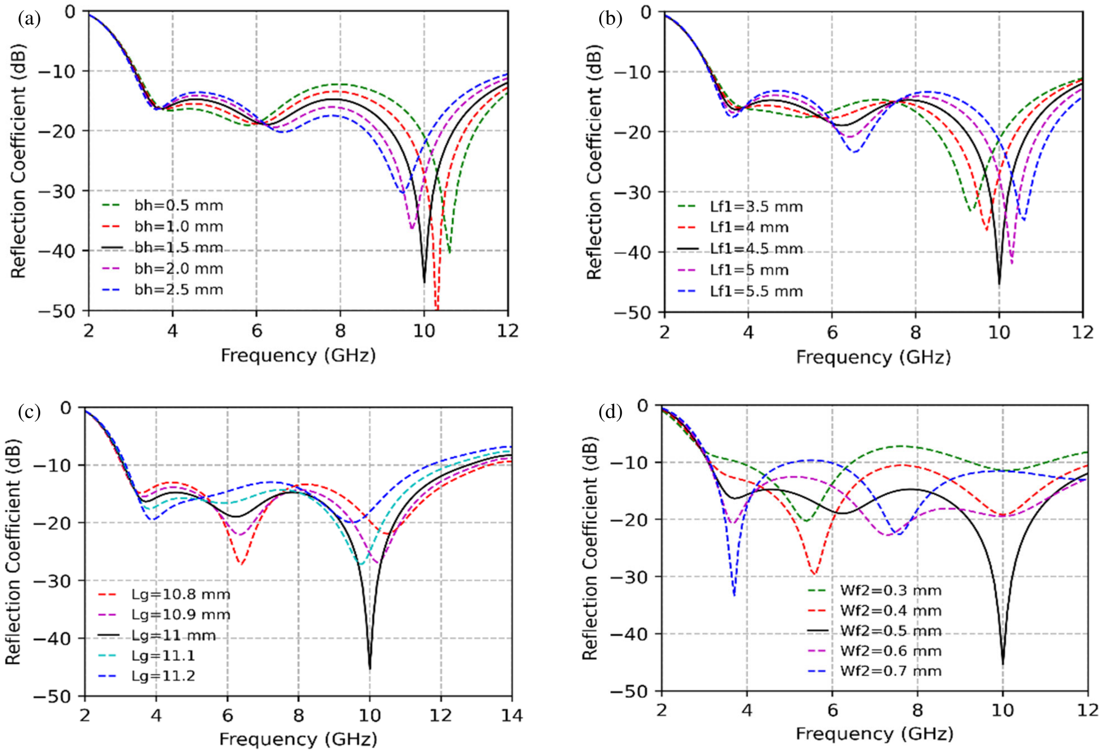

FIGURE 3. Variation of (a) bh, (b) L_{f1}, (c) L_g, and (d) W_{f2} on the performance of reflection coefficient.

foam (Y-bend). The foam cylinder has a dielectric constant of $\varepsilon_r = 1.03$.

Figure 4(a) shows the simulated and measured reflection coefficient curves of the proposed conformal UWB antenna in three scenarios: flat, bent along the X-axis, and bent along the Y-axis, along with their measurement setup. The measured lower edge frequencies are 3.11 GHz, 3.14 GHz, and 3.12 GHz for the flat position, X-axis bend, and Y-axis bend, respec-

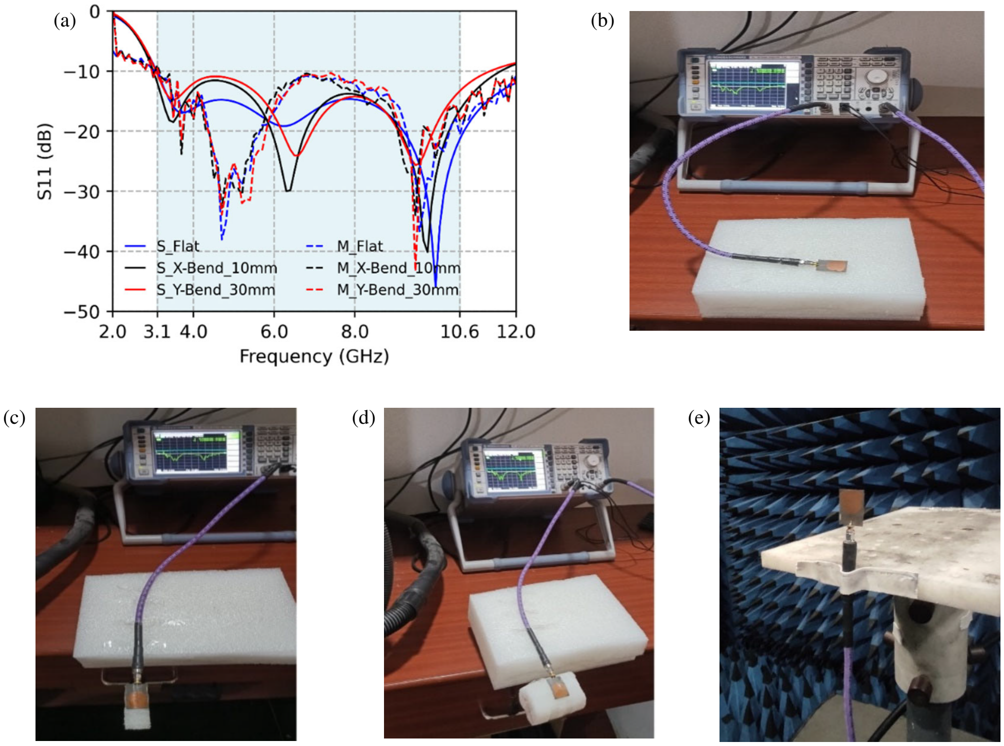

FIGURE 4. (a) Simulated vs. measured reflection coefficients for flat, X-bend, and Y-bend, measurement set up for (b) flat, (c) X-bend, (d) Y-bend, (e) far field parameters.

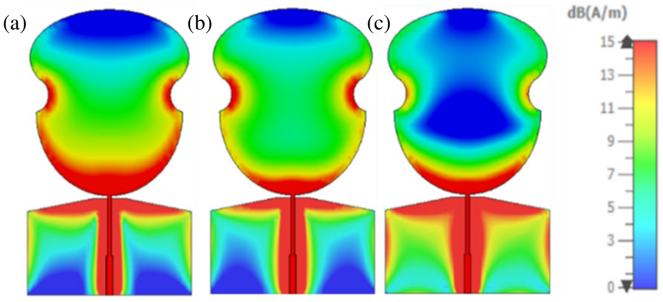

FIGURE 5. Surface current density distribution at frequencies of (a) 3.6 GHz, (b) 6.1 GHz, and (c) 9.9 GHz.

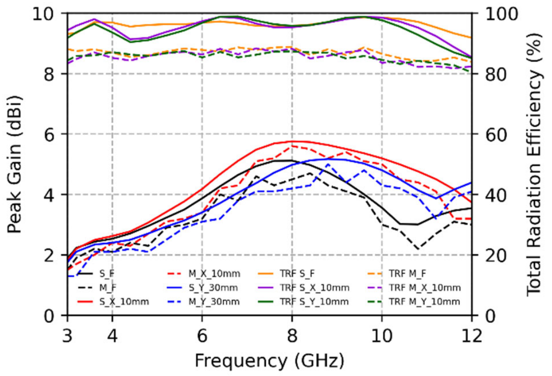

FIGURE 6. Simulated vs. measured peak gain and total radiation efficiency curves for flat, X-bend, and Y-bend.

tively, while the upper edge frequencies consistently extend beyond 10.6 GHz. This demonstrates good agreement between the simulated and measured results. Figures 4(b)–(d) illustrate the measurement setup for S-parameters under flat, X-bend, and Y-bend configurations using a Vector Network Analyzer (VNA). Figure 4(e) shows the measurement setup for far-field parameter measurements in an anechoic chamber.

Figure 5 depicts the surface current density flow on the UWB antenna at the selected discrete frequencies of 3.6 GHz, 6.1 GHz, and 9.9 GHz. At 3.6 GHz, the current is maximum around the perimeter of the structure, indicating a longer current path associated with lower frequencies. At 6.1 GHz, the current becomes less concentrated in the middle, reflecting a shorter path as the frequency increases. At 9.9 GHz, the current shifts further toward the bottom edges, signifying an even shorter path for the current at higher frequencies. This indicates how the current path shortens as the operating frequency increases.

Figure 6 depicts the simulated and measured peak gain and total radiation efficiency plots for various antenna configurations. In the flat configuration, the antenna achieved a measured peak gain of 4.7 dBi and a maximum total radiation efficiency of 88.8%. When bent along the X-axis, the measured peak gain is 5.6 dBi, and the maximum total radiation efficiency is 88.3%. Similarly, bending along the Y-axis resulted in a peak gain of 5 dBi and a maximum total radiation efficiency of 87.4%.

Figure 7 depicts normalized 2D radiation patterns from simulations and measurements at specific frequencies in the XZ and YZ planes for flat, X-bend, and Y-bend geometries. The antenna exhibits a bidirectional pattern in the YZ plane and an

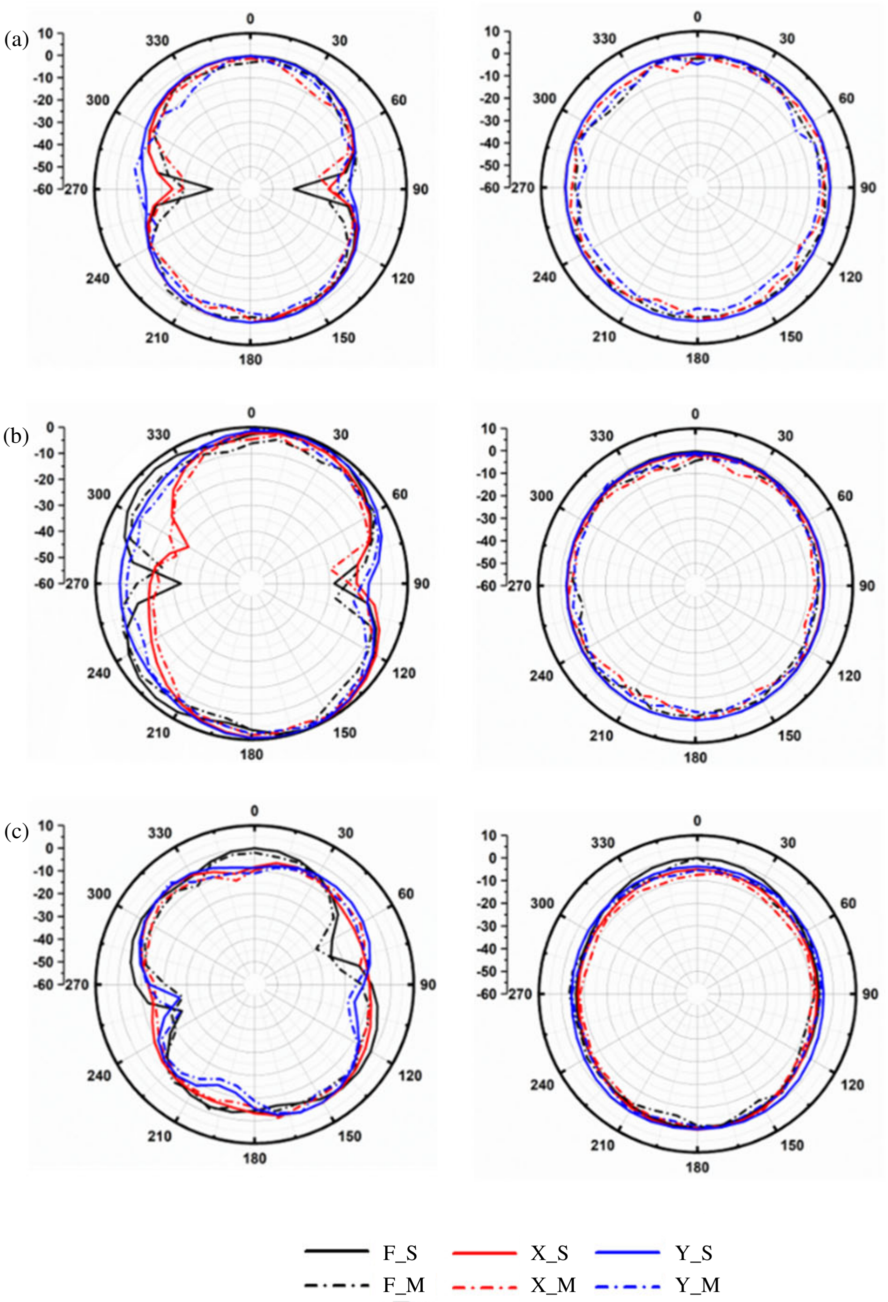

FIGURE 7. Simulated and measured 2D radiation patterns at (a) 3.6 GHz, (b) 6.1 GHz, and (c) 9.9 GHz.

omnidirectional pattern in the XZ plane. Bending modifies the bidirectional pattern in the YZ plane. Overall, the simulated and measured results align closely, with only slight differences.

2.1. Time Domain Analysis of UWB Antenna

To evaluate the time-domain performance of the proposed conformal UWB antenna, two identical antennas are placed at a minimum separation distance determined by Eq. (2). The assessment is performed for three configurations: Flat, X-bend, and Y-bend, in both face-to-face and side-by-side orientations.

$$R = 2D^2/\lambda \tag{2}$$

where D is the largest antenna dimension, and λ is the wavelength at the lower edge frequency. For the proposed antenna, with $D = 33$ mm and λ at 3 GHz, R is approximately obtained as 32.3 mm. In this study, during the simulation and measurement setup D is taken as 500 mm. Commonly used time domain metrics such as system fidelity factor (SFF), group delay, and transmission coefficient responses are considered.

2.1.1. Group Delay

It represents the signal delay in free space and is theoretically described as $\tau_g(\omega) = -d\phi(\omega)/d\omega$. Figure 8(a) shows that the simulated group delay remains constant across the UWB in all three configurations. However, the Y-bend arrangement has the highest measured deviation, up to 2 ns, whereas the other configurations have a maximum deviation of less than 1.4 ns.

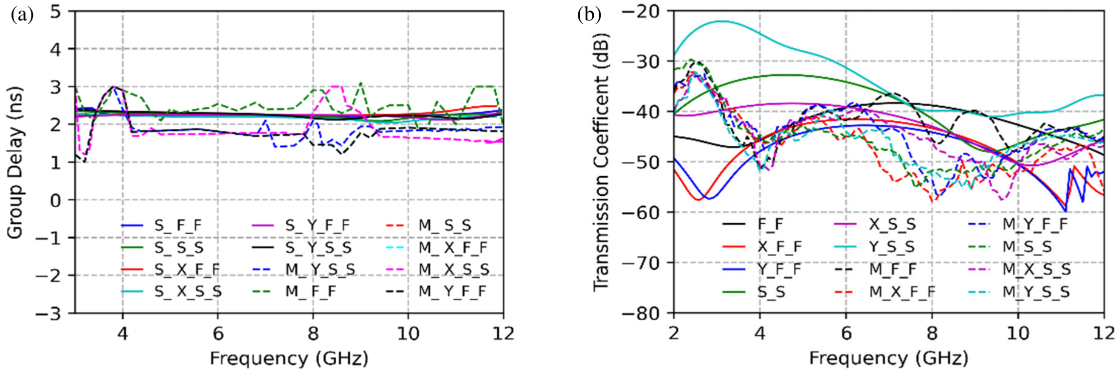

FIGURE 8. Simulated versus measured (a) group delay and (b) transmission coefficient responses for flat, X-bend, and Y-bend configurations.

This indicates minimum signal distortion and the antenna's dependable operation.

2.1.2. Transmission Coefficient

Figure 8(b) demonstrates the simulated and measured transmission coefficient responses for the discussed three cases. It is observed that the measured transmission coefficients remain well below -30 dB across the UWB range.

2.1.3. SFF

It investigates the antenna's temporal and spatial behavior. To evaluate the system fidelity factor, a 5th-order Gaussian pulse is considered as a transmitted signal that complies with the FCC's spectrum mask for UWB communications. Its PSD is illustrated in Figure 9. The 5th-order Gaussian pulse is given by Eq. (3).

$$T_s(t)=C\left(-\frac{t^5}{\sqrt{2\pi}\sigma^{11}}+10\,\frac{t^3}{\sqrt{2\pi}\sigma^{9}}-15\,\frac{t}{\sqrt{2\pi}\sigma^{7}}\right)e^{\left(-\frac{t^2}{2\sigma^2}\right)} \tag{3}$$

SFF can be evaluated by using the formula below

$$\mathrm{SFF} = \max_{n}\int_{-\infty}^{\infty}\hat{T}_s(t)\hat{R}_s(t+\tau)dt \tag{4}$$

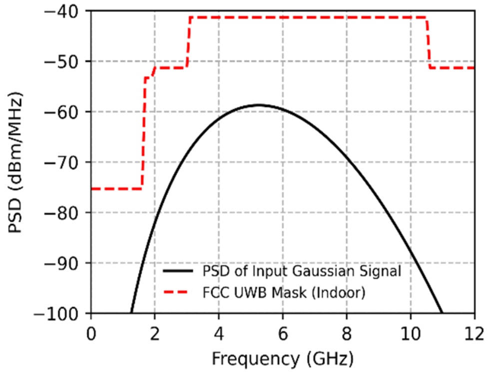

FIGURE 9. Power spectral density (PSD) of the 5th derivative Gaussian pulse.

$$\hat{R}_s(t) = \frac{R_s(t)}{\left[\int\limits_{-\infty}^{\infty}\left|R_s(t)\right|^2 dt\right]^{1/2}} \tag{5}$$

$$\hat{T}_s(t) = \frac{T_s(t)}{\left[\int\limits_{-\infty}^{\infty}\left|T_s(t)\right|^2 dt\right]^{1/2}} \tag{6}$$

The received signal is then computed by the following steps:

$$R_s(\omega) = \mathrm{FFT}(T_s(t))\cdot H(\omega) \tag{7}$$

$$R_s(t) = \mathrm{IFFT}(R_s(\omega)) \tag{8}$$

Here, $H(\omega)$ is taken from Figure 8(b).

Figure 10 depicts the received pulse waveforms for the UWB in the three configurations described before. The received signal closely matches the transmitted signal, with slight ringing effects appearing at the tail end. These ringing effects are due to the substrate material's energy storage properties or its potential deformation during bending.

The comparison of simulated and measured SFF values is given in Table 2. SFF value in all measured cases exceeds 80% which is better than the required minimum of 50%.

TABLE 2. Simulated and measured SFFs.

Case	% SFF (Simulated)	SFF Measured
F_F	91.3	86.7
X_F_F	92.1	85.3
Y_F_F	88.2	88.9
S_S	85.2	80.1
X_S_S	84.7	82.7
Y_S_S	83.1	81.2

Figure 11(a) depicts the equivalent circuit representation of the single antenna element using the degenerated Foster canonical (DFC) approach. This method models the antenna as a network of parallel RLC circuits, each covering a specific frequency bandwidth around its resonance. By overlapping these

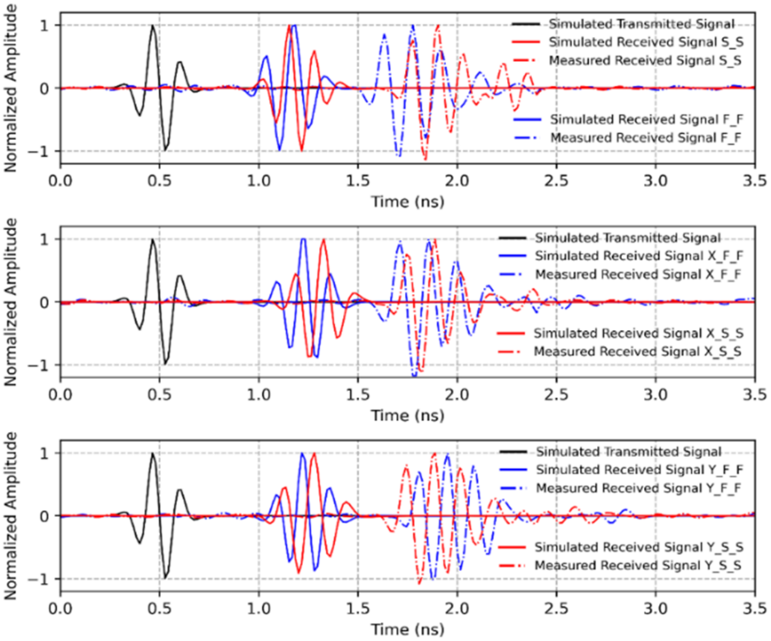

FIGURE 10. Simulated and measured transmitted and received 5th-order Gaussian signals.

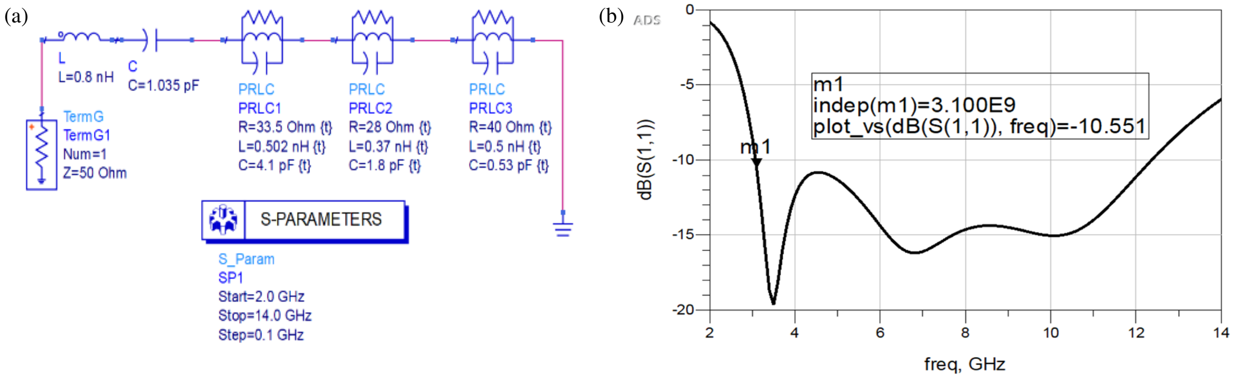

FIGURE 11. (a) Equivalent circuit model of the UWB antenna and (b) equivalent circuit model reflection coefficient.

bandwidths, the antenna achieves the desired wide bandwidth. The initial, middle, and final RLC circuits ensure impedance matching at low, mid, and high frequencies, respectively. Figure 11(b) illustrates the model's reflection coefficient curve, covering a bandwidth from 3.0 GHz to 12.4 GHz, with component values provided Figure 11(a).

3. FOUR ELEMENT MIMO ANTENNA DESIGN

Figure 12 displays the simulated model and fabricated prototype top and bottom layers of the 4-element MIMO antenna system, designed using the previously discussed single antenna element. The system consists of four antennas, designated as ANT-1, ANT-2, ANT-3, and ANT-4 arranged orthogonally with a separation distance of d to minimize mutual coupling and support polarization diversity. Thin L-shaped metallic stubs interconnect the grounds of four radiators via a square-shaped ring located at the center of the substrate's bottom surface. The MIMO antenna system measures $63 \times 63 \times 0.25\,\text{mm}^3$ overall.

Figure 13 depicts the evolution of the ground structure across three stages: Case 1 to Case 3. In Case 1, the ground planes of the radiating antenna elements remain isolated, with no interconnection. Cases 2 and 3 introduce square-shaped rings of varying dimensions to connect the ground planes. The graph shows that Case 3 offers a better transmission coefficient response than the previous two cases, especially at lower frequencies.

Figure 14 depicts the surface current density flow on radiating elements at various discrete frequencies, with and without connected ground planes. In this setup, ANT-1 is excited, while other antennas are terminated with a 50-ohm impedance. Figure 14(a) illustrates that the diagonally positioned antenna element, ANT-3, is affected by ANT-1, as indicated by the current distribution along the feedline. Due to this, the transmission coefficient curve S_{13} around 3.2 GHz is affected, as shown in Figure 13.

When the interconnected ground structure is incorporated into the design as shown in Figure 14(b), the magnitude of the current is lowered on the feedline of ANT-2, indicating im-

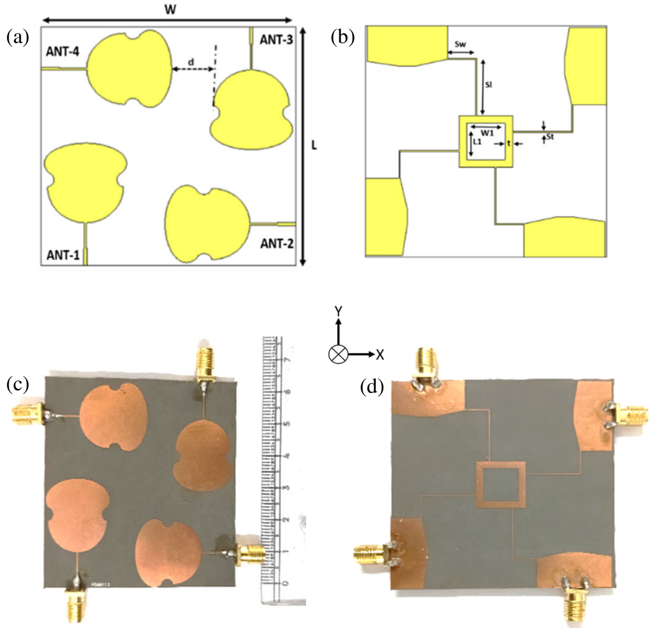

FIGURE 12. Proposed 4-element conformal UWB antenna layout. (a) Top view, (b) bottom view, (c) fabricated prototype top view, (d) fabricated prototype bottom view.

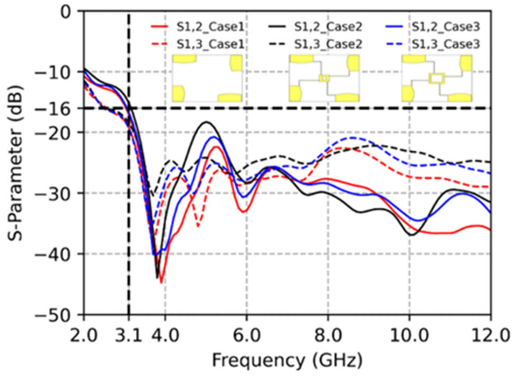

FIGURE 13. Inter connected ground plane evolutionary stages.

provement in the mutual coupling, and the same can be observed in Figure 13. However, ANT-2 and ANT-4 are lightly influenced by ANT-1. This effect is not much as their transmission coefficient responses are below −16 from Figure 13. The surface current density distribution on the radiating elements at 6.8 GHz and 9 GHz is presented in Figure 14(c) and Figure 14(d). At 6.8 GHz, significant surface current is observed on the ground plane of ANT-4; however, it does not affect the transmission coefficient response shown in Figure 13. At 9 GHz, there is minimal current distribution on the neighboring antennas, indicating good mutual coupling.

The S-parameters of the MIMO antenna system are measured using the Rohde & Schwarz vector network analyzer (VNA). As the VNA used is a 2-port device, ANT-1 and ANT-2 are connected to the two channels during the measurement, while the remaining ports of the MIMO antenna are terminated with 50 Ω-matched loads. This procedure is repeated for all port pairs.

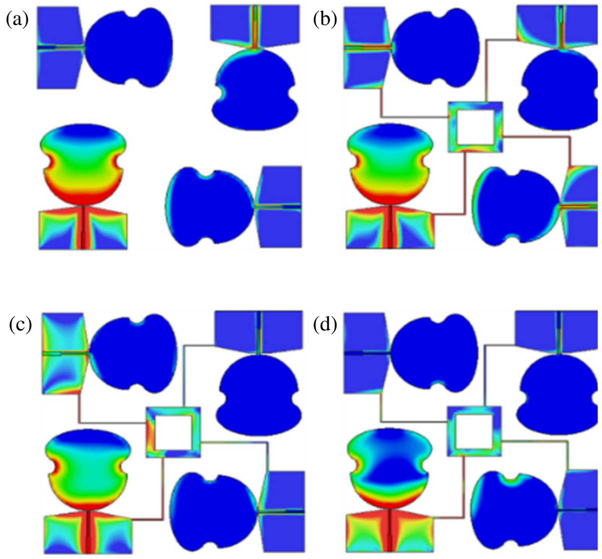

FIGURE 14. Surface current distribution on the 4-element UWB antenna, (a) without interconnected ground plane at 3.2 GHz, (b) with connected ground planes at 3.2 GHz, (c) with connected ground planes at 6.8 GHz, and (d) with connected ground planes at 9 GHz.

TABLE 3. Simulated and measured reflection coefficient bandwidths for flat and conformal cases.

Case	Antenna	Simulated Bandwidth (GHz)	Measured Bandwidth (GHz)
Flat	ANT-1	3.0 to > 12	3.4 to > 12
	ANT-2	3.0 to > 12	3.5 to 12
	ANT-3	3.0 to > 12	3.5 to > 12
	ANT-4	3.0 to > 12	3.5 to > 12
Conformal	ANT-1	2.95 to > 12	3.5 to > 12
	ANT-2	2.97 to > 12	3.3 to 10.8
	ANT-3	2.96 to > 12	3.4 to > 12
	ANT-4	2.97 to > 12	3.3 to > 12

Figure 15(a) presents the simulated and measured reflection coefficient curves for the proposed MIMO antenna system for both the flat and conformal configuration with a 40 mm bending radius. Figure 15(b) shows the transmission coefficient curves for the discussed configurations. It is observed that the transmission coefficient curves are below −18 dB. The simulated and measured bandwidths for these cases are summarized in Table 3. The discrepancies observed between the measured results are likely due to losses from SMA connectors, bending losses, and environmental factors during the measurements. Figures 15(c)–(d) show the MIMO antenna setup for S-parameter measurements under flat and conformal configurations using a VNA. Figure 15(e) presents the setup for far-field measurements in an anechoic chamber.

The equivalent circuit of the proposed four-element MIMO antenna system, along with its reflection coefficient response, is given in Figure 16. Each radiator is represented by three parallel RLC resonant circuits, while the L-shaped stubs are modeled as inductors. Each side of the square ring is realized with a

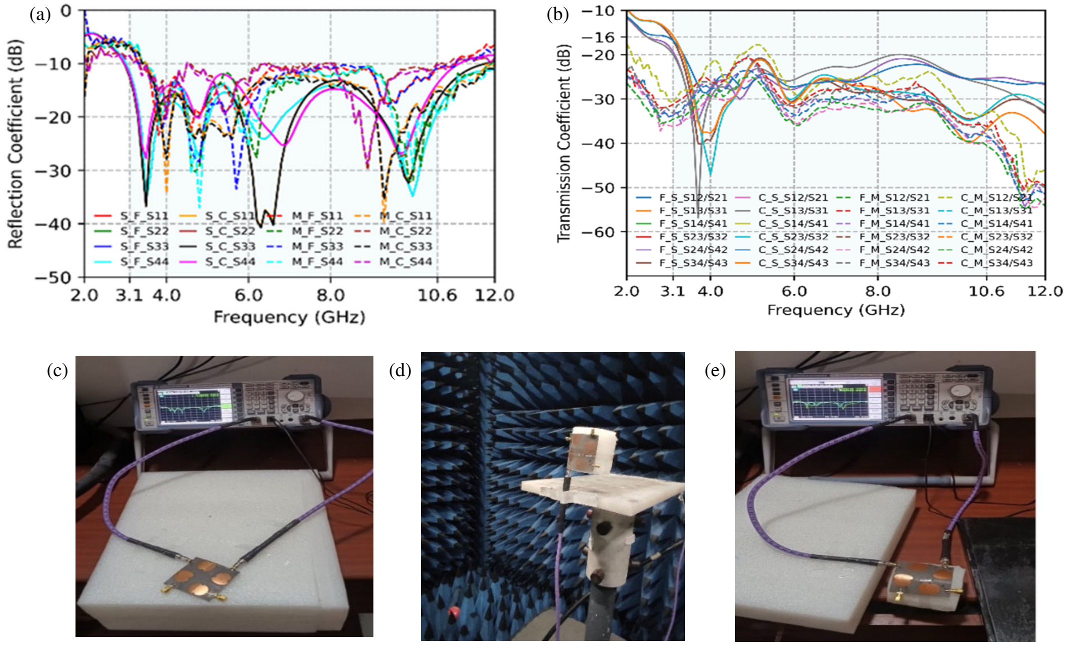

FIGURE 15. (a) Simulated and measured reflection coefficients, (b) simulated and measured transmission coefficient responses for flat and conformal configurations, measurement setup for (c) flat case, (d) conformal, (e) far-field.

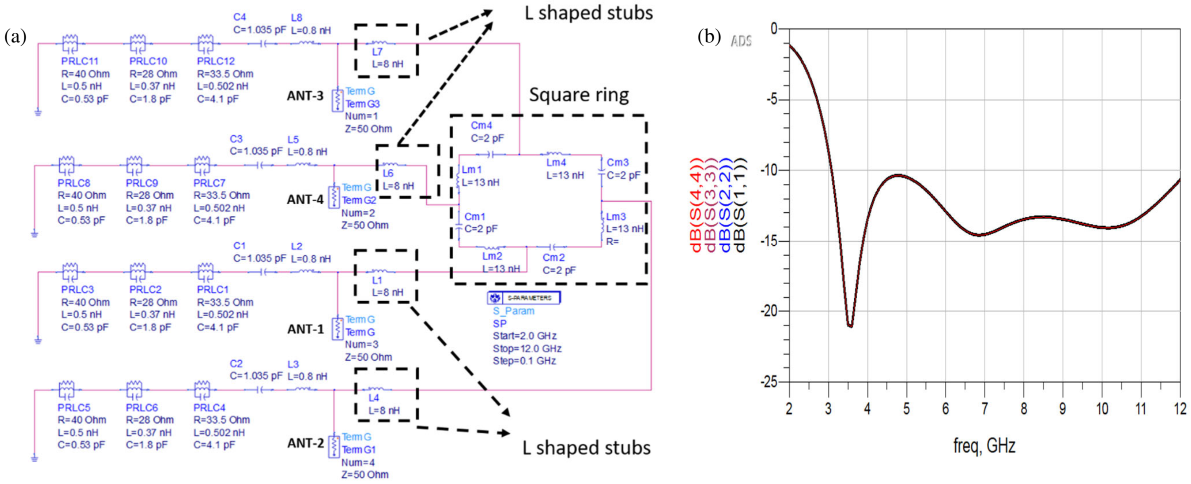

FIGURE 16. (a) Equivalent circuit diagram of the proposed 4 port flexible MIMO antenna system. (b) Reflection coefficient response curves of the equivalent circuit.

series of inductors and capacitors to achieve proper impedance matching and coupling. The circuit is simulated in advanced system design (ADS), and obtained reflection coefficient results closely match the reflection coefficient results obtained from CST MWS.

Figure 17 presents the normalized simulated and measured 2D radiation patterns at 3.6 GHz, 6.1 GHz, and 9.9 GHz in the XZ and YZ planes for the flat, X-bend, and Y-bend configurations. The proposed antenna exhibits an omnidirectional pattern. Bending the antenna causes a shift in the bidirectional radiation pattern in the YZ plane under the X-bend and Y-bend scenarios. It is also noted that measured and simulated patterns align closely, with minor acceptable differences.

3.1. MIMO Diversity Analysis

This section focuses on assessing the diversity performance of the proposed UWB MIMO antenna through an analysis of key metrics such as ECC, DG, MEG, CCL, and TARC [25, 32].

3.1.1. ECC

It measures the degree of correlation between the signals received at different antenna elements within a MIMO system. It is evaluated using Eq. (9). From Figure 18(a) it is observed that the measured ECC values are below 0.01 for both cases.

$$\mathrm{ECC}_{i,j} = \frac{\left|S_{ii}^{*}S_{ji} + S_{ji}^{*}S_{jj}\right|^2}{\left(1 - |S_{ii}|^2 - |S_{ji}|^2\right)\left(1 - |S_{jj}|^2 - |S_{ji}|^2\right)} \tag{9}$$

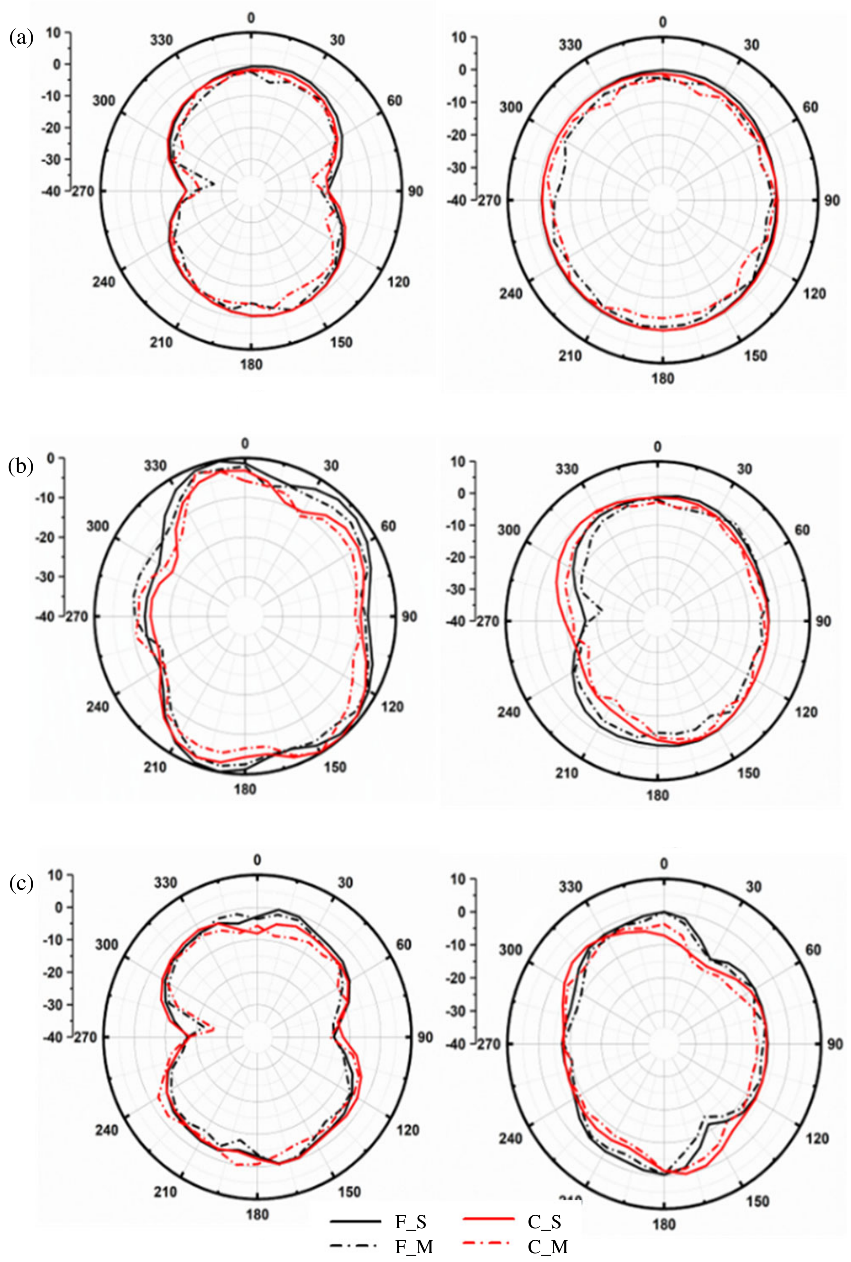

FIGURE 17. Simulated versus measured normalized 2D radiation patterns at (a) 3.6 GHz, (b) 6.1 GHz, and (c) 9.9 GHz.

3.1.2. DG

It measures the ability of the MIMO system to mitigate multipath fading and enhance signal reliability. Figure 18(b) illustrates the diversity gain of the proposed antenna for flat and conformal cases. All responses are approximately 10 dB, which corresponds to the ideal value. DG is calculated using Eq. (10).

$$DG_{i,j} = 10\sqrt{1 - \mathrm{ECC}_{i,j}^2} \tag{10}$$

3.1.3. CCL

It measures the reduction in channel capacity caused by signal correlation and mutual coupling between antenna elements. Figure 19(a) illustrates the CCL curves for flat and conformal configurations across different port pairs which are less than 0.4 bits/s/Hz.

$$C_{\mathrm{LOSS}} = -\log_2 \det(\Psi^R) \tag{11}$$

$$\Psi_{i,j}^R = \begin{pmatrix} \Psi_{ii} & \Psi_{ij} \\ \Psi_{ji} & \Psi_{jj} \end{pmatrix} \tag{12}$$

$$\text{Diagonal elements : } \Psi_{ii} = \left(1 - |S_{ii}|^2 - |S_{ji}|^2\right) \tag{13}$$

$$\text{Off Diagonal elements : } \Psi_{ij} = -(S_{ii}^* S_{ij} + S_{ji}^* S_{jj}) \tag{14}$$

3.1.4. MEG

It evaluates how effectively the antenna receives power in the presence of multipath propagation and spatial diversity. It is

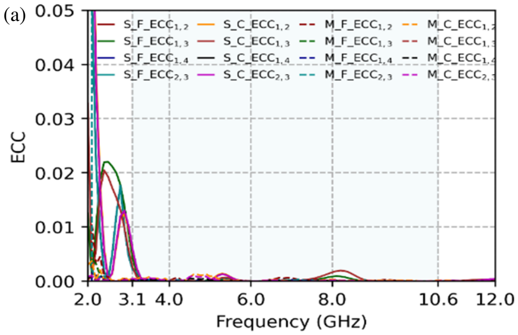

FIGURE 18. Simulated and measured (a) ECC and (b) DG responses for flat and bend configurations.

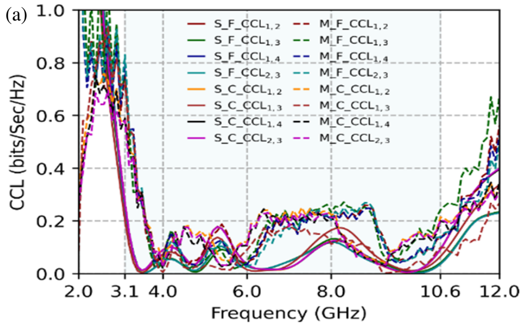

FIGURE 19. Simulated and measured (a) CCL and (b) MEG responses for flat and bend configurations.

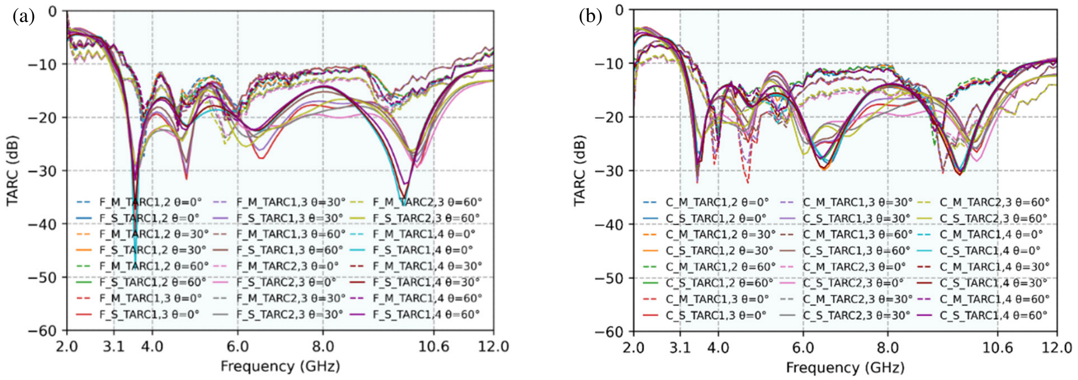

FIGURE 20. Simulated and measured TARC responses for (a) bend and (b) flat configurations.

evaluated using Eq. (15). MEG values of each port for the flat and conformal configurations are illustrated in Figure 19(b). The measured MEG values are nearly identical and lie between -6 dB and -12 dB.

$$\mathrm{MEG}_i = 0.5\left(1 - 0.5\sum_{j=1}^{N}|S_{ij}|^2\right) \tag{15}$$

MEG_i represents the Mean Effective Gain for port i, which consists of N antennas.

3.1.5. TARC

It measures the ratio of reflected power to incident power. The expression for TARC using S-parameters is given by Eq. (16). The phase angle θ takes values of 0°, 30°, and 60°. Figure 20 presents the measured and simulated TARC curves for both flat and conformal cases, demonstrating values below -10 dB from 3.4 GHz to 11 GHz.

$$\mathrm{TARC} = \frac{\sqrt{\left|S_{11} + S_{12}e^{j\theta}\right|^2 + \left|S_{21} + S_{22}e^{j\theta}\right|^2}}{\sqrt{2}} \tag{16}$$

From the comparison in Table 4, studies in [20, 21] focus on rigid MIMO antennas, limiting their use in conformal devices. Works in [22–30] explore four-element MIMO antennas on flexible substrates, but [22–27] lack time-domain analysis; [28] uses a semi-flexible FR4 substrate; and [29, 30] provide time-domain analysis in flat configuration only. Higher-order MIMO antennas in [13, 14] require more space and hardware. Thus, the proposed work achieves conformability and compact size, and evaluates key time-domain parameters such as group delay, S_{12}, and SFF, which are not comprehensively addressed in other works.

TABLE 4. Comparison of the proposed work with the literature.

Ref.	**Size (mm^3)**	**Substrate/ ε_r**	**BW (GHz)**	**Isolation (dB)**	**ECC**	**Flexibility**	**Technique/ method**	**No. of MIMO Elements/ common ground**	**Time domain analysis**
[13]	$39 \times 39 \times 0.8$	RT duroid 5880/2.2	2.3–21.7	> 16.3	< 0.001	Yes	Side by Side/Stub	2/Yes	No
[20]	$62.5 \times 60.5 \times 1.6$	Fr4/4.4	3.5–11	> 20	< 0.01	No	Orthogonal	4/No	YES, S_{12} Group delay
[21]	$38 \times 45 \times 1.6$	FR4/4.4	2–11	17	0.01	No	Face to Face stub	4/Yes	No
[22]	$72 \times 72 \times 0.8$	FR4/4.4	2.8–13.3	> 18	< 0.06	No	Orthogonal, stubs	4/Yes	No
[23]	$16 \times 71.5 \times 0.76$	RT duroid 5880/2.2	3.2–14	> 22	< 0.01	Yes	Side-by-Side	4/No	No
[24]	$65 \times 65 \times 0.1$	LCP/2.9	2.9–10.86	> 22	< 0.01	Yes	Orthogonal	4/No	No
[25]	$50 \times 50 \times 0.787$	Rogers 5880/2.8	2.2–10.4	> 14	< 0.3	Yes	Face to Face	4/Yes	No
[26]	$92 \times 92 \times 1.5$	Foam/2.5	2–14	> 20	NA	Yes	Orthogonal	4/Yes	No
[27]	$50 \times 50 \times 1.52$	RO3003/3	3–12	> 15	< 0.01	YES	Orthogonal	4/yes	NO
[28]	$56 \times 68 \times 0.2$	FR4/4.4	3.89–17.09	> 15	< 0.02	Yes	Face to Face	4/Yes	YES, S_{12} group delay
[29]	$40 \times 40 \times 0.05$	Polyimide /3.5	3.82–15.9	> 20	< 0.005	Yes	Orthogonal	4/Yes	YES, S_{12} group delay
[30]	$45 \times 55 \times 1$	PET/NA	3.19–9.30	> 20	< 0.02	YES	Face to Face	4/YES	YES, S_{12} Group delay
[14]	$71 \times 95 \times 1.6$	Fr4/4.4	2.9–11	> 20	< 0.075	No	Side by side & Face to Face/DGS	6/Yes	YES, S_{12} Group delay, SFF
[15]	$48 \times 48\times 1.6$	Fr4/4.4	2.5–24	> 22.5	< 0.3	No	conjoined reflector	8/Yes	YES, S_{12} Group delay
[16]	100×100(3D)	Fr4/4.4	1.7–1.9, 2.35–2.55, 3–12	> 20	< 0.28	No	3D arrangement	12/Yes	No
Pr.	$63 \times 63 \times 0.254$	RT duroid 5880/2.2	3.5–10.8	> 18	< 0.01	Yes	Orthogonal	4/Yes	YES, S_{12} Group delay, SFF

4. CONCLUSION

A conformal antenna system with four elements has been designed, fabricated, and tested for UWB applications. A flexible guitar-shaped conformal UWB antenna, serving as a single antenna element, is thoroughly analyzed in both time and frequency domains for flat, X-bend, and Y-bend configurations using simulated and measured results. The measured results demonstrate a -10 dB impedance bandwidth ranging from 3.14 GHz to beyond 10.6 GHz, a peak gain of 5.6 dB, a maximum total radiation efficiency of 87.4%, an omnidirectional radiation pattern, an SFF exceeding 80%, and a maximum group delay deviation of 2 ns. A 4-element conformal MIMO antenna system was developed based on the single antenna element, with a prototype fabricated and tested. It offers a -10 dB impedance bandwidth from 3.5 GHz to 10.8 GHz and mutual coupling below -18 dB. The system shows excellent diversity performance, with an ECC under 0.01, a DG of nearly 10 dB, a MEG between -6 dB and -12 dB, a CCL below 0.4 bits/s/Hz, and a TARC below -10 dB across the 3.4 GHz to 11 GHz range. The results confirmed that the antenna maintained stable performance even when being subjected to bending, ensuring its effectiveness in flexible UWB portable devices.

REFERENCES

[1] Federal Communications Commission, "Revision of Part 15 of the commission's rules regarding ultra-wideband transmission systems," *First Report and Order FCC 02-48*, Washington, DC, 2002.

[2] Foschini, G. J. and M. J. Gans, "On limits of wireless communications in a fading environment when using multiple antennas," *Wireless Personal Communications*, Vol. 6, No. 3, 311–335, 1998.

[3] Nella, A. and A. S. Gandhi, "A survey on planar antenna designs for cognitive radio applications," *Wireless Personal Communications*, Vol. 98, 541–569, 2018.

[4] Jhunjhunwala, V. K., T. Ali, P. Kumar, P. Kumar, P. Kumar, S. Shrivastava, and A. A. Bhagwat, "Flexible UWB and MIMO antennas for wireless body area network: A review," *Sensors*, Vol. 22, No. 23, 9549, 2022.

[5] Saeidi, T., I. Ismail, W. P. Wen, A. R. H. Alhawari, and A. Mohammadi, "Ultra-wideband antennas for wireless communication applications," *International Journal of Antennas and Propagation*, Vol. 2019, No. 1, 7918765, 2019.

[6] Khaleel, H. R., H. M. Al-Rizzo, D. G. Rucker, and S. Mohan, "A compact polyimide-based UWB antenna for flexible electronics," *IEEE Antennas and Wireless Propagation Letters*, Vol. 11, 564–567, 2012.

[7] Koohestani, M., N. Pires, A. K. Skrivervik, and A. A. Moreira, "Time-domain performance of patch-loaded band-reject UWB antenna," *Electronics Letters*, Vol. 49, No. 6, 385–386, 2013.

[8] Koohestani, M., A. A. Moreira, and A. K. Skrivervik, "System fidelity factor evaluation of wearable ultra-wideband antennas for on-body communications," *IET Microwaves, Antennas & Propagation*, Vol. 9, No. 10, 1054–1058, 2015.

[9] Valizade Shahmirzadi, N. and H. Oraizi, "Frequency- and time-domain analysis of a novel reconfigurable microstrip antenna for UWB applications," *Journal of Electromagnetic Waves and Applications*, Vol. 30, No. 17, 2311–2324, 2016.

[10] Wang, L., Z. Du, H. Yang, R. Ma, Y. Zhao, X. Cui, and X. Xi, "Compact UWB MIMO antenna with high isolation using fence-type decoupling structure," *IEEE Antennas and Wireless Propagation Letters*, Vol. 18, No. 8, 1641–1645, 2019.

[11] Singh, G., S. Kumar, B. K. Kanaujia, and V. K. Pandey, "Design and implementation of a compact tri-band four-port multiple-input-multiple-output antenna," *International Journal of RF and Microwave Computer-Aided Engineering*, Vol. 32, No. 8, e23218, 2022.

[12] Wang, L., Z. Du, H. Yang, R. Ma, Y. Zhao, X. Cui, and X. Xi, "Compact UWB MIMO antenna with high isolation using fence-type decoupling structure," *IEEE Antennas and Wireless Propagation Letters*, Vol. 18, No. 8, 1641–1645, 2019.

[13] Khedr, A. A., B. E. Elnaghi, and A. M. Mohamed, "Design of a compact dual port 2 × 1 ultra-wideband MIMO antenna for radio frequency energy harvesting based on four "A" shaped slots," *Progress In Electromagnetics Research M*, Vol. 128, 41–49, 2024.

[14] Kumar, P., S. Pathan, O. P. Kumar, S. Vincent, Y. Nanjappa, P. Kumar, P. Shetty, and T. Ali, "Design of a six-port compact UWB MIMO antenna with a distinctive DGS for improved isolation," *IEEE Access*, Vol. 10, 112 964–112 974, 2022.

[15] Mohanty, A. and S. Sahu, "Design of 8-port compact hybrid fractal UWB MIMO antenna with a conjoined reflector-ground integration for isolation improvement," *AEU — International Journal of Electronics and Communications*, Vol. 145, 154102, 2022.

[16] Kannappan, L., S. K. Palaniswamy, M. Kanagasabai, P. Kumar, M. G. N. Alsath, S. Kumar, T. R. Rao, M. Marey, A. Aggarwal, and J. K. Pakkathillam, "3-D twelve-port multi-service diversity antenna for automotive communications," *Scientific Reports*, Vol. 12, No. 1, 403, 2022.

[17] Nadeem, I. and D.-Y. Choi, "Study on mutual coupling reduction technique for MIMO antennas," *IEEE Access*, Vol. 7, 563–586, 2018.

[18] Kumar, A., A. Q. Ansari, B. K. Kanaujia, J. Kishor, and L. Matekovits, "A review on different techniques of mutual coupling reduction between elements of any MIMO antenna. Part 1: DGSs and parasitic structures," *Radio Science*, Vol. 56, No. 3, 1–25, 2021.

[19] Sharawi, M. S., "Current misuses and future prospects for printed multiple-input, multiple-output antenna systems [wireless corner]," *IEEE Antennas and Propagation Magazine*, Vol. 59, No. 2, 162–170, 2017.

[20] Abdelghany, M. A., M. F. A. Sree, A. Desai, and A. A. Ibrahim, "4-port octagonal shaped MIMO antenna with low mutual coupling for UWB applications," *Computer Modeling in Engineering & Sciences*, Vol. 136, No. 2, 1999–2015, 2023.

[21] Thakur, E., N. Jaglan, and S. D. Gupta, "Miniaturized four-port UWB MIMO antennas with triple-band rejection using single EBG structures," *International Journal of Microwave and Wireless Technologies*, Vol. 14, No. 2, 185–193, 2022.

[22] Kumar, S., G. H. Lee, D. H. Kim, W. Mohyuddin, H. C. Choi, and K. W. Kim, "Multiple-input-multiple-output/diversity antenna with dual band-notched characteristics for ultra-wideband applications," *Microwave and Optical Technology Letters*, Vol. 62, No. 1, 336–345, 2020.

[23] Rao, P. K. and R. Mishra, "Elliptical shape flexible MIMO antenna with high isolation for breast cancer detection application," *IETE Journal of Research*, Vol. 69, No. 1, 325–333, 2023.

[24] Zhang, J., C. Du, and R. Wang, "Design of a four-port flexible UWB-MIMO antenna with high isolation for wearable and IoT applications," *Micromachines*, Vol. 13, No. 12, 2141, 2022.

[25] Liu, H., G. Kang, and S. Jiang, "Compact dual band-notched UWB multiple-input multiple-output antenna for portable applications," *Microwave and Optical Technology Letters*, Vol. 62, No. 3, 1215–1221, 2020.

[26] Jayant, S., G. Srivastava, and S. Kumar, "Quad-port UWB MIMO footwear antenna for wearable applications," *IEEE Transactions on Antennas and Propagation*, Vol. 70, No. 9, 7905–7913, 2022.

[27] Aboelleil, H., A. A. M. Khalaf, and A. A. Ibrahim, "Quad ports flexible MIMO antenna with connected ground and high isolation for UWB applications," *Analog Integrated Circuits and Signal Processing*, Vol. 120, No. 1, 59–70, 2024.

[28] Desai, A., J. Kulkarni, M. M. Kamruzzaman, S. Hubálovský, H.-T. Hsu, and A. A. Ibrahim, "Interconnected CPW fed flexible 4-port MIMO antenna for UWB, X, and Ku band applications," *IEEE Access*, Vol. 10, 57 641–57 654, 2022.

[29] Rajesh, G. and R. Poonkuzhali, "Design and analysis of CPW fed ultrathin flexible MIMO antenna for UWB and X-band applications," *IEEE Access*, Vol. 12, 96 704–96 717, 2024.

[30] Desai, A., H.-T. Hsu, B. M. Yousef, A. M. Ameen, Y.-F. Tsao, and A. A. Ibrahim, "UWB connected ground transparent 4-port flexible MIMO antenna for IoT applications," *IEEE Internet of Things Journal*, Vol. 11, No. 7, 12 475–12 484, 2024.

[31] Agrawall, N. P., G. Kumar, and K. P. Ray, "Wide-band planar monopole antennas," *IEEE Transactions on Antennas and Propagation*, Vol. 46, No. 2, 294–295, 1998.

[32] Singh, G., S. Kumar, B. K. Kanaujia, and V. K. Pandey, "Design and performance analysis of a frequency reconfigurable four-element multiple-input-multiple-output antenna," *AEU — International Journal of Electronics and Communications*, Vol. 146, 154118, 2022.